# Chapter 4
# Iris Recognition

"[The iris] consists of pectinate ligaments adhering into a tangled mesh revealing striations, ciliary processes, crypts, rings, furrows, a corona, sometimes freckles, vasculature, and other features."

John Daugman, in *Biometrics: Personal Identification in Networked Society (Jain et al.)*, 1999

The rich texture of the iris can be used as a biometric cue for person recognition. The richness and variability observed in the iris texture is due to the agglomeration of multiple anatomical entities composing its structure. Due to the presence of distinctive information at multiple scales, a wavelet-based signal processing approach is commonly used to extract features from the iris. One of the most popular approaches to iris recognition generates a binary code to represent and match pairs of irides. First, a segmentation routine is used to detect the iris region in the ocular image captured by the camera. Next, a geometric normalization method is used to transform the nearly annular iris region into a rectangular entity. Then, this rectangular entity is convolved with a Gabor filter resulting in a complex response, and the phase information of the ensuing response is quantized into a binary code, commonly referred to as the iris code. Finally, Hamming distance is used to compare two iris codes and generate a match score, which is used for biometric recognition. This chapter discusses the salient aspects of a typical iris recognition system.

## 4.1 Introduction

The use of the ocular region as a biometric trait has gained impetus, especially due to significant advancements made in iris recognition since 1993. The ocular region of the human face consists of the eyes and the surrounding structures such as facial skin, eyebrows, and nose bridge (Figure 4.1). While various components of the eye have been proposed as biometric indicators (viz., iris, retina, and conjunctival vasculature), it is the iris that has been extensively studied in the biometrics literature and used in large-scale biometric systems.

The iris is an internal organ of the eye that is located just behind the cornea and in front of the lens. The primary function of the iris is to regulate the amount of light entering the eye by dilating or contracting a small opening in it called the pupil. The iris contracts the pupil when the ambient illumination is high and dilates it when the

A.K. Jain et al., *Introduction to Biometrics*, DOI 10.1007/978-0-387-77326-1_4,

**Fig. 4.1** The ocular region of the human face includes the eyes, eyebrows, nose bridge, and facial skin. The iris is the colored structure located in the annular region of the eye and is bounded by the pupil (the dark opening in the eye) and the sclera (the white of the eye). When viewed in detail, even the left iris and the right iris of an individual exhibit significant differences in their texture, although some global similarities may be observed. It must be noted that a typical iris recognition system does not use the color of the iris for human recognition.

illumination is low. The iris is a multilayered structure and a cross-section of the iris reveals the following layers:

- The posterior layer at the back, which is two cells thick, contains heavily pigmented epithelial cells, making it impenetrable to light.
- The muscle layer above it consists of the sphincter and dilator muscles that contract and dilate the pupil.
- The stromal layer, located above the muscles, is made up of collagenous connective tissue (arranged in an arch-like configuration) and blood vessels (arranged along the radial direction).
- The anterior border layer is the foremost layer and has an increased density of chromatophores (i.e., pigment containing cells) compared to the stromal layer.

The anterior portion of the iris - consisting collectively of the muscles, stroma, and the border layers - is the foremost visible portion of the iris. Therefore, it can be imaged by a camera and is the focus of all automated iris recognition systems. Figure 4.2 shows an image of the iris as viewed by a near-infrared camera. The iris, from this perspective, appears as an annular entity bound by the pupillary boundary (that separates it from the dark pupil) and the limbus boundary (that separates it from the white sclera).

The iris image is partitioned into two zones: the central pupillary zone and the surrounding ciliary zone. These two zones are divided by a circular zigzag ridgeline known as the collarette. Many pit-like irregular structures appear mainly in the region around the collarette. These structures are called crypts (Fuchs crypts) and they permit fluids to quickly enter and exit the iris during dilation and contraction of the pupil. Near the outer part of the ciliary zone, concentric lines can be seen,

especially in case of darkly pigmented irides[1]. These lines become deeper as the pupil dilates and are called contraction furrows. In the pupillary zone, radial furrows are observed.

The agglomeration of the aforementioned structures imparts a rich texture to the iris. The term *texture* denotes the characteristics of an image in terms of its homogeneity, coarseness, regularity, directionality, etc. The biometric literature indicates that the iris exhibits substantial diversity in its texture across the population. The uniqueness of each iris is assumed to be a consequence of the random morphogenesis of its textural relief during prenatal growth. Even the irides of monozygotic twins exhibit differences in their texture, thereby suggesting that these patterns are determined epigenetically by random events during development that impact the morphogenesis of the tissue. Using the terminology developed in Chapter 1, the iris texture is predominantly a phenotypic trait with limited genetic penetrance.

The color of the iris is primarily defined by the pigmentation present in it. The pigmentation itself is controlled by the number of melanin granules - a genetically determined factor. However, other factors, such as the cellular density of the stroma, can also affect the color of the iris. As will be explained later, the color of the iris does *not* play a significant role in iris recognition systems. It is the texture detail present in the anterior portion of the iris that is useful for recognition.

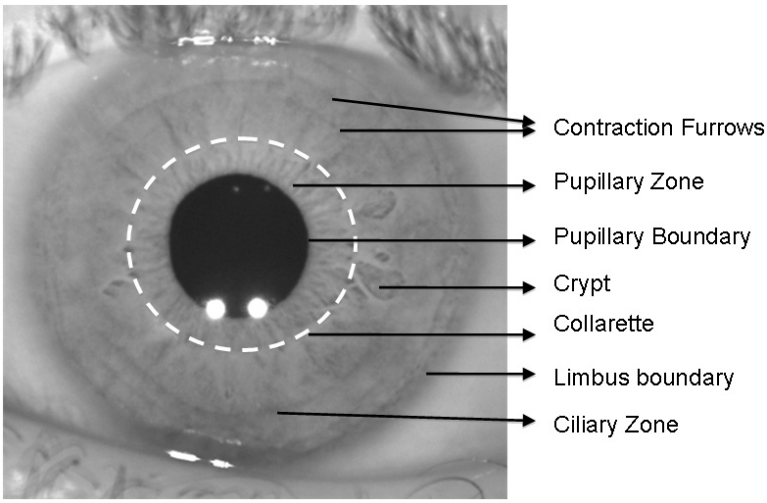


**Fig. 4.2** Anatomy of the iris as observed by a near-infrared camera placed in front of the eye. The rich texture of the iris is due to its anterior portion consisting of the musculature, stroma, and the anterior border layers. When the anterior border layer recedes, the collarette becomes visible as a zig-zag line separating the ciliary zone from the pupillary zone. Crater-like irregular structures called crypts are often observed when the anterior layer thins out, thereby revealing the heavily pigmented and much darker posterior layer.

[1] The plural form of iris is *irides* although the term *irises* has also been extensively used in the biometric literature.

## 4.2 Design of an Iris Recognition System

An iris recognition system may be viewed as a pattern matching system whose goal is to compare two irides and generate a match score indicating their degree of similarity or dissimilarity. Thus, a typical iris recognition system has four different modules: the acquisition, segmentation, normalization, and encoding/matching modules. Figure 4.3 indicates the flow of information in a typical iris recognition system.

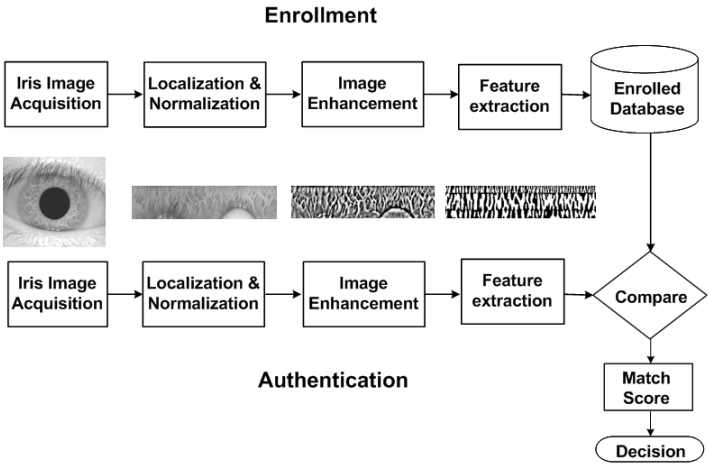


**Fig. 4.3** The block diagram of an iris recognition system. The matching performance of an iris recognition system can be impacted by the accuracy of the segmentation module, which detects the iris and establishes its spatial extent in an image of the ocular region.

1. *Acquisition*: The role of the acquisition module is to obtain a 2D image of the eye using a monochrome CCD camera that is sensitive to the near-infrared (NIR) range of the electromagnetic spectrum. An external source of NIR light, often co-located with the acquisition system, is used to illuminate the iris. Most iris recognition systems require the participating individual to be cooperative and to place their eye in close proximity to the camera. The system typically captures a series of images of the eye and, based on a quality evaluation scheme, retains only a few images that are deemed to have sufficient iris texture information for further processing.
2. *Segmentation*: The segmentation module localizes the spatial extent of the iris in the image of the eye by isolating it from other structures present in its vicinity. These structures include the sclera, the pupil, the eyelids, and the eyelashes. Typically, segmentation is accomplished by detecting the inner and outer boundaries of the iris (commonly referred to as the pupillary boundary and the limbus boundary, respectively), and the eyelids and eyelashes that can interrupt the circular contour of the limbus boundary. The integro-differential operator, explained

later, is commonly used to detect the boundaries of the iris, although, more recently, the use of active contours has been proposed in order to account for the case when the boundaries cannot be represented as a simple conic section such as a circle or an ellipse. Iris segmentation is a critical component of any iris biometric system; inaccuracies in localizing the iris can severely impact the matching accuracy of the system, thereby undermining its utility.

3. *Normalization*: Once the inner and outer boundaries of the iris are estimated, a geometric normalization scheme is invoked to transform the iris texture within the annular region from cartesian coordinates to pseudo polar coordinates via a rubber sheet model. This process is often alluded to as the "unwrapping of the iris" and it results in a rectangular entity whose rows correspond to the angular direction in the original iris and whose columns correspond to its radial direction. The purpose of this exercise is three-fold: (a) it accounts for variations in pupil size that can impact the spatial extent of the iris; (b) since the size of the pupil can vary across the population, the normalization scheme ensures that the irides of different individuals are mapped into a common image domain; and (c) during the matching stage, two normalized irides can be registered by a simple translation operation that can account for the tilting of the head during the image acquisition process. Associated with each unwrapped iris is a binary mask that labels valid iris pixels with a "1", thereby separating them from pixels corresponding to the eyelids and eyelashes that are identified in the segmentation module and assigned a label "0". Geometric normalization is followed by some photometric transformations that enhance the textural structure of the unwrapped iris.
4. *Encoding and Matching*: While the unwrapped iris may be directly used to compare two irides (e.g., by using correlation filters), typically a feature extraction routine is used to encode its textural content. Most encoding algorithms perform a multi-resolution analysis of the iris by applying wavelet filters and examining the ensuing response. A commonly used encoding mechanism uses quadrature 2D Gabor Wavelets to extract the local phasor information of the iris texture. Each phasor response (the magnitude of the response is not used) is then encoded using two bits of information based on the quadrant of the complex plane in which it lies. The resulting 2D binary code is referred to as the iris code. Two such iris codes can be compared using the Hamming distance, which computes the number of corresponding bits that are different across them; the binary mask computed in the segmentation module is used to ensure that only bits corresponding to valid iris pixels are compared. Prior to computing the Hamming distance, a registration procedure may be necessary to align the two iris codes.

Each of these modules is described in detail in the subsequent sections of this chapter.

Figure 4.4 shows two important applications of an iris recognition system. The first application is the use of iris recognition at airports for recognizing passengers, employees, and flight crews where high accuracy as well as fast processing are crucial, especially when matching an individual against a watch list. The second application is the use of iris recognition in a coal mine. Note that the individuals

working in a coal mine may not be able to provide good quality fingerprints or face images due to the working conditions.

## 4.3 Image Acquisition

An image of the eye is obtained using a sensor that is sensitive to the near-infrared (NIR) portion of the electromagnetic spectrum. This typically corresponds to the 700nm - 900nm range of the infra-red (IR) spectral band. The use of a NIR sensor has at least two distinct advantages:

- First, the textural nuances of dark-colored irides are not clearly resolved in the visible[2] portion of the electromagnetic spectrum due to the absorption characteristics of the melanin that is found in the iris. Therefore, color images of dark-colored irides do not clearly reveal the rich texture of the iris. Increasing the wavelength of the illuminant aids in the better penetration of the anterior portion of dark-colored irides, thereby divulging these complex patterns. The use of NIR illumination along with a NIR sensor is, therefore, preferred in order to elicit textural details on the surface of the iris. This is illustrated in Figure 4.5. The three rows in this figure correspond to three different irides acquired using a multispectral camera. This camera captures the red, green, blue, and NIR spectra of each iris. The top row depicts a dark brown iris, the middle row a green iris, and the bottom row a light-blue iris. As can be seen in this figure, the textural details of the dark-brown iris are more evident in the NIR channel than in the red, green, or blue channels.
- Second, NIR light cannot be perceived by the human eye. This ensures that the image acquisition process is non-intrusive, even when the eye is required to be in close proximity to the sensor and the NIR light source. Typically, the source of NIR illumination is in the proximity of the subject to ensure that the illumination power is not unduly large as this can be harmful to the eye.

Most systems acquire a series of NIR eye images from the subject and utilize quality measures to choose a subset of images (often just 1 image) for further processing. Most iris recognition systems expect 100 - 200 pixels across the iris in the radial direction for successful processing. Images of the iris can, however, be negatively impacted by several factors, including partially closed eyelids, intruding eyelashes, harsh or non-uniform illumination, low resolution, and extremely dilated or constricted pupil. By appropriately controlling the ambient illumination and requiring subjects to interact with the system in a co-operative manner, some of these conditions can be avoided. Figure 4.6 shows sample images of the eye taken from three publicly available iris databases.

[2] Regular digital cameras typically record images in the visible spectrum. Such images are referred to as *color* images or *RGB* images. RGB refers to Red, Green and Blue - three primary colors that can be mixed appropriately to generate other colors. Thus, a digital color image is composed of three different channels - RGB - that pertain to the visible portion of the electromagnetic spectrum.


(a)

(b)

**Fig. 4.4** Practical examples of iris recognition systems. (a) The iris recognition system used in UAE for identifying expellees attempting to re-enter the country. (b) An iris recognition system being used in a coal mine in China.

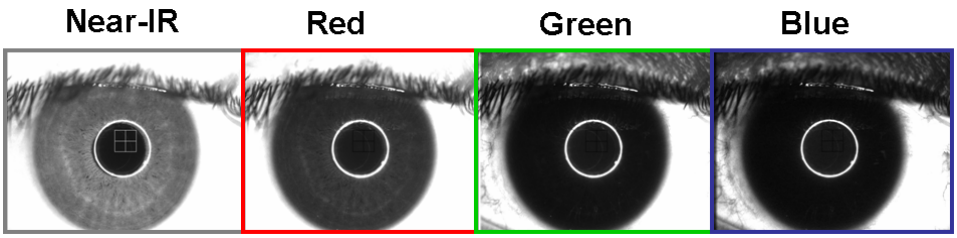


(a) Dark brown colored iris

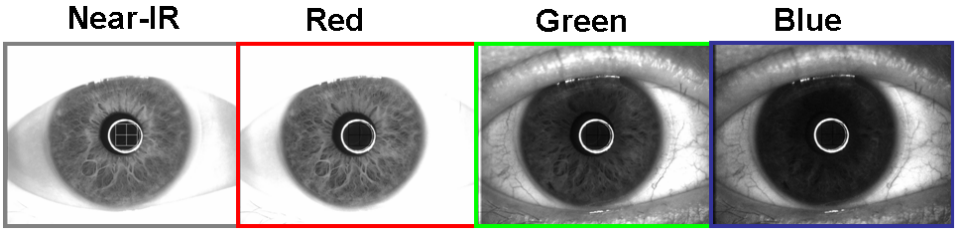


(b) Green colored iris

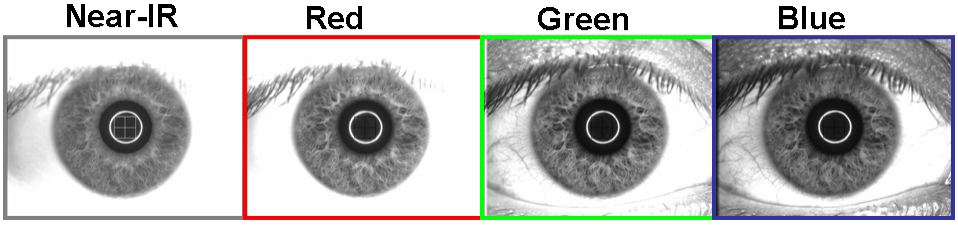


(c) Blue colored iris

**Fig. 4.5** The texture revealed in three different irides when they are observed in the NIR, red, green, and blue channels. (a) A dark brown colored iris, (b) a green colored iris, and (c) a blue colored iris. The color of the iris was visually assessed by a human. Notice that in (a), the texture of the iris is not clearly resolved in the red, green, and blue channels; however, it is better resolved in the NIR channel. On the contrary, in (c), the texture of the iris is reasonably resolved in all 4 channels. Thus, the use of the NIR channel for iris recognition is particularly beneficial for dark colored irides.

A number of commercial iris capture devices are currently available. Figure 4.7 lists a few examples. The Panasonic BM-ET 330 is a portable device weighing about 5 lbs and has a range between 11.8 and 15.7 inches. It can obtain images of both eyes simultaneously. The LG Iris Access 4000 has an auto-focus lens and is also able to acquire images of both eyes simultaneously. It can be wall-mounted and has an operating distance between 10.2 and 14.2 inches. The IRISPASS-M, which weighs about 11 lbs, can also be wall-mounted and has an operational range between 1-2 feet. MobileEyes is a hand-held tethered dual-eye capture device that weighs about 2.8 lbs. The IGH1000 is a hand-held iris device (however, it can be wall-mounted

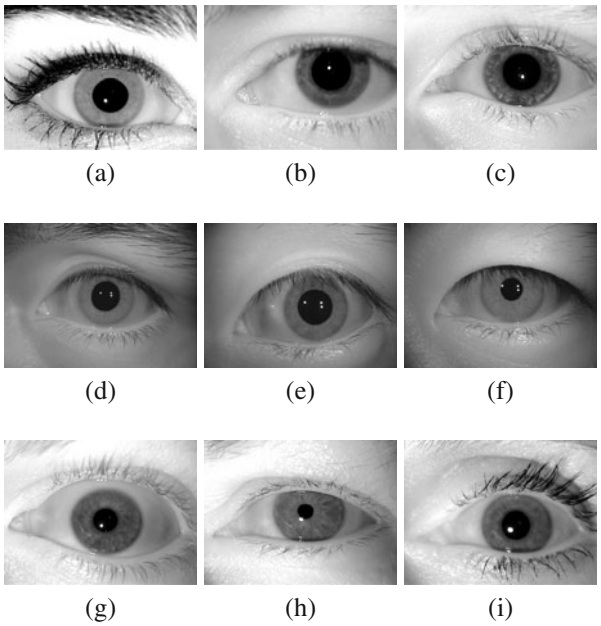


**Fig. 4.6** Iris images from the ICE (top row), CASIA version 3 (middle row) and MBGC (bottom row) databases. All these images were acquired in the NIR spectrum. The ICE and MBGC images were obtained using the LG EOU 2200 camera, while the CASIA version 3 images were obtained using the OKI IRISPASS device.

as well) that weighs only 750 g. It has a focal distance between 4.7 and 11.8 inches, and captures the image of a single eye.

In all the above devices, the subject's eye has to be relatively stable and in close proximity to the camera. However, more recent research has explored the possibility of acquiring iris scans from moving subjects who are at a considerable distance from the acquisition device (see Figure 4.8). This represents a daunting task, since the iris is a slightly oscillating object (due to the hippus movements initiated by its muscles) within a moving object (the eye-ball), which is located within yet another moving object (the head)! Further, the device has to be equipped with lenses having a long focal length (e.g., 8 inches). An appropriately designed choke-point[3] can ensure that the subject's gaze is directed toward the iris camera while simultaneously activating the NIR illuminant present in the vicinity of the choke-point. The versatility of current iris recognition systems will be substantially enhanced if the iris image can be acquired from non-cooperative subjects in challenging environments characterized by harsh illumination and large stand-off distances.

[3] An example would be a portal that constrains the subject's gaze and regulates their walking speed


**Fig. 4.7** Examples of commercialized iris image acquisition devices: (a) Panasonic BM-ET 330, (b) LG IrisAccess 4000, (c) Datastrip Easy Verify, (d) Oki IrisPass, (e) Retica MobileEyes, and (f) IrisGuard IGH1000. Most iris acquisition devices require the subject to be extremely cooperative and situated at a short distance from the camera. Specialized NIR lighting is necessary to illuminate the eye during image acquisition.


(a) (b)

**Fig. 4.8** Examples of Iris On the Move (IOM) systems: (a) Pass Thru, and (b) Passport Portal. IOM systems can potentially facilitate the covert acquisition of eye images for iris recognition.

## 4.4 Iris Segmentation

An iris camera captures an image of the eye that, besides the iris, includes the pupil, eyelids, eyelashes, and sclera. As seen in Figure 4.6, the iris is perceived to be located in the vicinity of these structures in a 2D image of the eye. The process of locating and isolating the iris from such an image is known as iris localization or segmentation. The primary task of segmentation is to determine pixels in the image that correspond to the iris region.

Iris segmentation is not an easy task for the following reasons:

- The iris texture exhibits a great degree of irregularity and its textural content varies substantially across eyes. Indeed, the iris could be viewed as a stochastic texture containing numerous "edge" like features that are randomly distributed on its anterior surface. Simple image models cannot be used to describe its content, thereby precluding the use of appearance-based schemes (i.e., schemes that model the iris texture based on its visual appearance) for iris localization.
- The iris is an annular-like structure bounded by the pupil in its internal perimeter, and the sclera and eyelids in its external perimeter. Incorrectly estimating these boundaries (contours) can result in the over-segmentation or under-segmentation of the iris entity. In some eye images, these boundaries (especially the limbus boundary) may not be very sharp, thereby affecting the accuracy of the boundary estimation process. Further, the boundary defined by the eyelids is irregularly shaped.
- The iris texture may be partially occluded by eyelashes. The eyelashes protruding into the iris image can generate spurious edges and affect the segmentation process.

The contrast in image intensity between the pupil and the iris offers a good cue for identifying the pupillary boundary[4]. Similarly, the contrast between the iris and the sclera can be used to detect the limbus boundary, although the magnitude of the intensity gradient across the limbus boundary may be stronger than that of the pupillary boundary in NIR images. One of the most commonly used methods in iris segmentation relies on the detection of these boundaries. It assumes that (a) both these boundaries can be approximated using circles, and (b) the magnitude of the edge pixels contributing to these boundaries is stronger than those pertaining to other circular contours in the image. The entire operation can be summarized using an integro-differential operator as described below.

### *4.4.1 Segmentation using the integro-differential operator*

The integro-differential operator, qualified by the order statistic (max), is of the form

$$max(r, x_0, y_0)\left|G_\sigma(r) * \frac{\partial}{\partial r}\oint_{r,x_0,y_0}\frac{I(x,y)}{2\pi r}ds\right|. \tag{4.1}$$

Here, $I$ is the input eye image and $I(x,y)$ is the pixel intensity of the image at location $(x,y)$. According to Equation (4.1), the given image $I$ is convolved with a radial Gaussian filter $G_\sigma(r)$ of scale $\sigma$ and radius $r$. This is essential to ensure that sharp edges corresponding to crypts, freckles, and furrows are reasonably blurred. Next, using a circle of radius $r$ and centered at $(x_0, y_0)$ in the image, the intensity gradient of those pixels lying on the circumference of this circle is computed. For each pixel, the gradient is computed along the line connecting it to the center of the circle; this is denoted by the differential operator $\frac{\partial}{\partial r}$. The sum of these gradient values, along the perimeter of the circle and normalized by the factor $2\pi r$, is then computed. This is denoted by the integral operator $\oint_{r,x_0,y_0}$ in Equation (4.1). The parameters $(r, x_0, y_0)$ that result in the maximum sum is assumed to define the circular contour of the pupillary boundary.

A similar procedure is used to detect the limbus boundary. However, in this case, the arc of integration is constrained to the near-vertical pixels on the circumference of the circle. This is necessary since the contour of the limbus may be interrupted by the upper and lower eyelids and, therefore, the effect of those pixels that do not belong to the limbus boundary has to be minimized. Figure 4.9 illustrates the output of this segmentation routine. In the eye image on the left, the limbus contour is not interrupted by the eyelids. Thus, the annular region defined by the two boundaries contains only those pixels corresponding to the iris. However, in the eye image on the right, both the pupillary and limbus contours are interrupted by the eyelids. Hence, a post-processing step is necessary to identify the eyelid boundaries and, subsequently, isolate those pixels within the annular region that correspond to the iris. It must be noted that the centers of the pupillary and limbus boundaries are typ-

[4] This contrast is relatively low for eyes afflicted with cataract.

ically different, i.e., the iris is not necessarily concentric with the pupil. In fact, the pupil center is nasal (i.e., shifted toward the nose bridge) and inferior to (i.e., below) the iris center.

The eyelids can be detected by searching for a parabolic edge within the region defined by the outer circle. Typically, a spline-fitting procedure is used to accomplish this. It is also possible to detect the eye-lashes infringing into the iris texture by searching for strong near-vertical edges in the segmented iris.

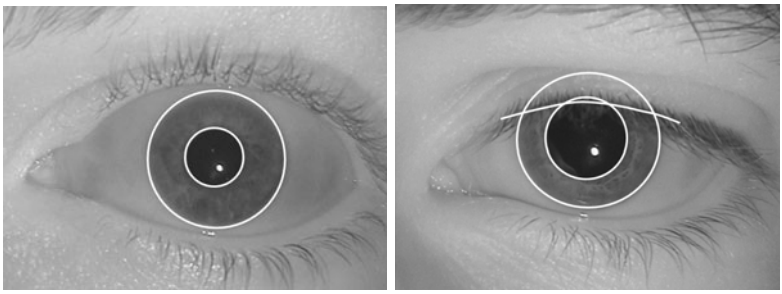

(a) (b)

**Fig. 4.9** Iris segmentation using the integro-differential operator. White lines are used to denote the output of the circle fitting algorithm. (a) An eye image in which the pupillary and limbus boundaries are not interrupted by the eyelids, and (b) an eye image in which the two boundaries are observed to be interrupted by the eyelids. In the case of (b), a post-processing scheme is required to detect the eyelids and extract the iris pixels from the annular region defined by the two circular contours.

### *4.4.2 Segmentation using Geodesic Active Contours (GAC)*

The integro-differential operator described above (and its variants) assume that the outer boundary of the iris can be approximated using a circle or an ellipse. However, as noted earlier, the presence of eyelid boundaries and eyelashes in the image may necessitate the application of a post-processing scheme to detect these entities *after* using the integro-differential operator. Alternately, a single contour-fitting method that simultaneously demarcates the iris from the sclera as well as the eyelids/eyelashes can be used. This is possible by adopting active contour methods that can detect irregular boundaries. In this subsection, the use of Geodesic Active Contours (GAC) to detect the outer boundary of the iris will be described.

This approach is based on the relation between active contours and the computation of geodesics (minimal length curves). The strategy is to evolve an arbitrarily initialized curve from within the iris under the influence of geometric properties of the iris boundary. GACs combine the energy minimization approach of the classical "snakes" and the geometric active contours based on curve evolution.

Let $\gamma(t)$ be the curve, that has to gravitate toward the outer boundary of the iris, at a particular time $t$. The time $t$ corresponds to the iteration number. Let $\psi$ be a function measuring the signed distance from the curve $\gamma(t)$. That is, $\psi(x,y)$ = distance of point $(x,y)$ to the curve $\gamma(t)$.

$$\psi(x,y) = \begin{cases} 0 & \text{if (x,y) is on the curve;} \\ < 0 & \text{if (x,y) is inside the curve;} \\ > 0 & \text{if (x,y) is outside the curve.} \end{cases} \tag{4.2}$$

Here, $\psi$ is of the same dimension as that of the eye image $I(x,y)$. The curve $\gamma(t)$ is called the level set of the function $\psi$. Level sets are the set of all points in $\psi$ where $\psi$ is some constant. Thus $\psi = 0$ is the zeroth level set, $\psi = 1$ is the first level set, and so on. $\psi$ is the implicit representation of the curve $\gamma(t)$ and is called the embedding function since it embeds the evolution of $\gamma(t)$. The embedding function evolves under the influence of image gradients and the region's characteristics so that the curve $\gamma(t)$ approaches the desired boundary of the iris. The initial curve $\gamma(t)$ is assumed to be a circle of radius $r$ just beyond the pupillary boundary. Let the curve $\gamma(t)$ be the zeroth-level set of the embedding function. This implies that

$$\frac{d\psi}{dt} = 0.$$

By the chain rule,

$$\frac{d\psi}{dt} = \frac{\partial\psi}{\partial x}\frac{dx}{dt} + \frac{\partial\psi}{\partial y}\frac{dy}{dt} + \frac{\partial\psi}{\partial t},$$

i.e.,

$$\frac{\partial\psi}{\partial t} = -\nabla\psi.\gamma\prime(t),$$

where $\nabla$ is the gradient operator. Splitting the $\gamma\prime(t)$ in the normal $(N(t))$ and tangential $(T(t))$ directions,

$$\frac{\partial\psi}{\partial t} = -\nabla\psi.(v_N N(t) + v_T T(t)).$$

Now, since $\nabla\psi$ is perpendicular to the tangent to $\gamma(t)$,

$$\frac{\partial\psi}{\partial t} = -\nabla\psi.(v_N N(t)). \tag{4.3}$$

The normal component is given by

$$N = \frac{\nabla\psi}{\|\nabla\psi\|}.$$

Substituting this in Equation (4.3),

$$\frac{\partial \psi}{\partial t} = -v_N \|\nabla \psi\|.$$

Let $v_N$ be a function of the curvature of the curve $\kappa$, stopping function $K$ (to stop the evolution of the curve) and the inflation force $c$ (to evolve the curve in the outward direction) such that,

$$\frac{\partial \psi}{\partial t} = -(div(K\frac{\nabla \psi}{\|\nabla \psi\|}) + cK)\|\nabla \psi\|.$$

Thus, the evolution equation for $\psi_t$[5] such that $\gamma(t)$ remains the zeroth level set is given by

$$\psi_t = -K(c + \varepsilon\kappa)\|\nabla \psi\| + \nabla \psi.\nabla K, \tag{4.4}$$

where, $K$, the stopping term for the evolution, is an image dependant force and is used to decelerate the evolution near the boundary; $c$ is the velocity of the evolution; $\varepsilon$ indicates the degree of smoothness of the level sets; and $\kappa$ is the curvature of the level sets computed as

$$\kappa = -\frac{\psi_{xx}\psi_y^2 - 2\psi_x\psi_y\psi_{xy} + \psi_{yy}\psi_x^2}{(\psi_x^2 + \psi_y^2)^{\frac{3}{2}}}.$$

Here, $\psi_x$ is the gradient of the image in the $x$ direction; $\psi_y$ is the gradient in the $y$ direction; $\psi_{xx}$ is the $2^{nd}$ order gradient in the $x$ direction; $\psi_{yy}$ is the $2^{nd}$ order gradient in the $y$ direction; and $\psi_{xy}$ is the $2^{nd}$ order gradient, first in the $x$ direction and then in the $y$ direction. Equation (4.4) is the level set representation of the geodesic active contour model. This means that the level-set $C$ of $\psi$ is evolving according to

$$C_t = K(c + \varepsilon\kappa)\mathbf{N} - (\nabla K.\mathbf{N})\mathbf{N} \tag{4.5}$$

where $N$ is the normal to the curve. The term $\kappa\mathbf{N}$ provides the smoothing constraints on the level sets by reducing their total curvature. The term $c\mathbf{N}$ acts like a balloon force and it pushes the curve outward towards the object boundary. The goal of the stopping function is to slow down the evolution when it reaches the boundary. However, the evolution of the curve will terminate only when $K = 0$, i.e., near an ideal edge. In most images, the gradient values will be different along the edge, thus requiring the use of different K values. In order to circumvent this issue, the third geodesic term $((\nabla K.\mathbf{N}))$ is necessary so that the curve is attracted toward the boundary ($\nabla K$ points toward the middle of the boundary). This term makes it possible to terminate the evolution process even if (a) the stopping function has different values along the edges, and (b) gaps are present in the stopping function.

The stopping term used for the evolution of level sets is given by

$$K(x,y) = \frac{1}{1 + (\frac{\|\nabla(G(x,y) \star I(x,y))\|}{k})^{\alpha}} \tag{4.6}$$

[5] The subscript $t$ denotes the iteration number

where $I(x,y)$ is the image to be segmented, G(x,y) is a Gaussian filter, and $k$ and $\alpha$ are constants. As can be seen, $K(x,y)$ is not a function of $t$.

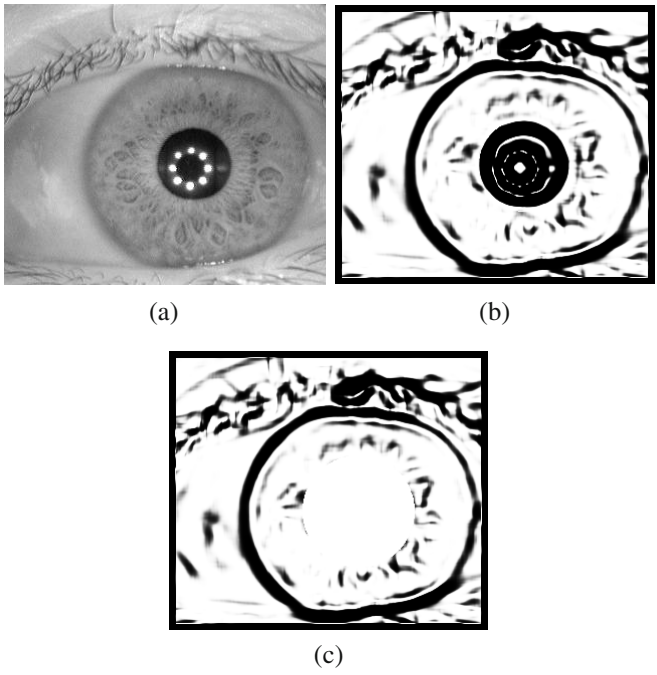

(a) (b)

(c)

**Fig. 4.10** Stopping function for the geodesic active contours. (a) Original iris image, (b) stopping function $K$, and (c) modified stopping function $K'$.

Consider an iris image to be segmented as shown in Figure 4.10 (a). The stopping function $K$ obtained from this image is shown in Figure 4.10 (b) (for $k = 2.8$ and $\alpha = 8$). Assuming that the inner iris boundary (i.e., the pupillary boundary) has already been detected, the stopping function $K$ is modified by deleting the circular edges corresponding to the pupillary boundary, resulting in a new stopping function $K'$. This ensures that the evolving level set is not terminated by the edges of the pupillary boundary (Figure 4.10 (c)).

A contour is first initialized near the pupil (Figure 4.11 (a)). The embedding function $\psi$ is initialized as a signed distance function to $\gamma(t=0)$ which looks like a cone (Figure 4.11 (b)). Discretizing equation 4.4 leads to the following equation:

$$\frac{\psi_{i,j}^{t+1} - \psi_{i,j}^{t}}{\Delta t} = -cK'_{i,j}\|\nabla\psi^t\| - K'_{i,j}(\varepsilon\kappa_{i,j}^{t}\|\nabla\psi^t\|) + \nabla\psi_{i,j}^{t}.\nabla K_{i,j}^{'t}, \qquad (4.7)$$

where $\Delta t$ is the time step (e.g., $\Delta t$ can be set to 0.05). The first term ($cK'_{i,j}\|\nabla\psi^t\|$) on the right hand side of the above equation is the velocity term (advection term) and, in the case of iris segmentation, acts as an inflation force. This term can lead to

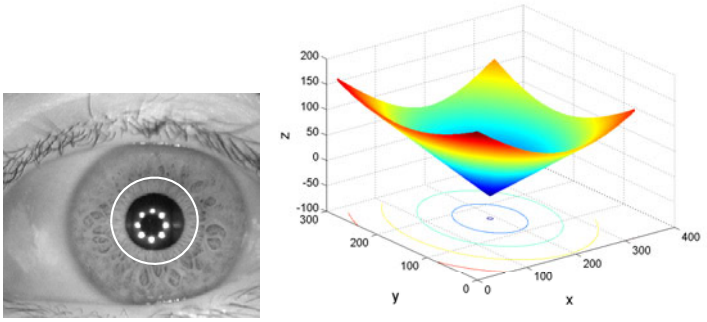


(a) (b)

**Fig. 4.11** Contour initialization for iris segmentation using GAC. (a) Zeroth level set (initial contour), (b) mesh plot denoting the signed distance function $\psi$.

singularities and hence is discretized using upwind finite differences. The upwind scheme for approximating $\|\nabla\psi\|$ is given by

$$\|\nabla\psi\| = \sqrt{A},$$
$$A = min(D_x^- \ \psi_{i,j}, 0)^2 + max(D_x^+ \ \psi_{i,j}, 0)^2 +$$
$$min(D_y^- \ \psi_{i,j}, 0)^2 + min(D_y^+ \ \psi_{i,j}, 0)^2.$$

$D_x^- \ \psi$ is the first order backward difference of $\psi$ in the x-direction; $D_x^+ \ \psi$ is the first order forward difference of $\psi$ in the x-direction; $D_y^- \ \psi$ is the first order backward difference of $\psi$ in the y-direction; and $D_y^+ \ \psi$ is the first order forward difference of $\psi$ in the y-direction. The second term $(K'_{i,j}(\varepsilon\kappa^t_{i,j}\|\nabla\psi^t\|))$ is a curvature based smoothing term and can be discretized using central differences. In our implementation, $c$ = 0.65 and $\varepsilon$ = 1 for all iris images. The third geodesic term $(\nabla\psi^t_{i,j}.\nabla K'^t_{i,j})$ is also discretized using the central differences.

After evolving the embedding function $\psi$ according to Equation (4.7), the curve begins to grow until it satisfies the stopping criterion defined by the stopping function $K'$. But at times, the contour continues to evolve in a local region of the image where the stopping criterion is not strong. This leads to over-evolution of the contour. This can be avoided by minimizing the thin plate spline energy of the contour. By computing the difference in energy between two successive contours, the evolution scheme can be regulated. If the difference between the contours is less than a threshold (indicating that the contour evolution has stopped at most places), then the contour evolution process is terminated. The evolution of the curve and the corresponding embedding functions are illustrated in Figure 4.12.

Since the radial fibers may be thick in certain portions of the iris, or the crypts present in the ciliary region may be unusually dark, this can lead to prominent edges in the stopping function. If the segmentation technique is based on parametric

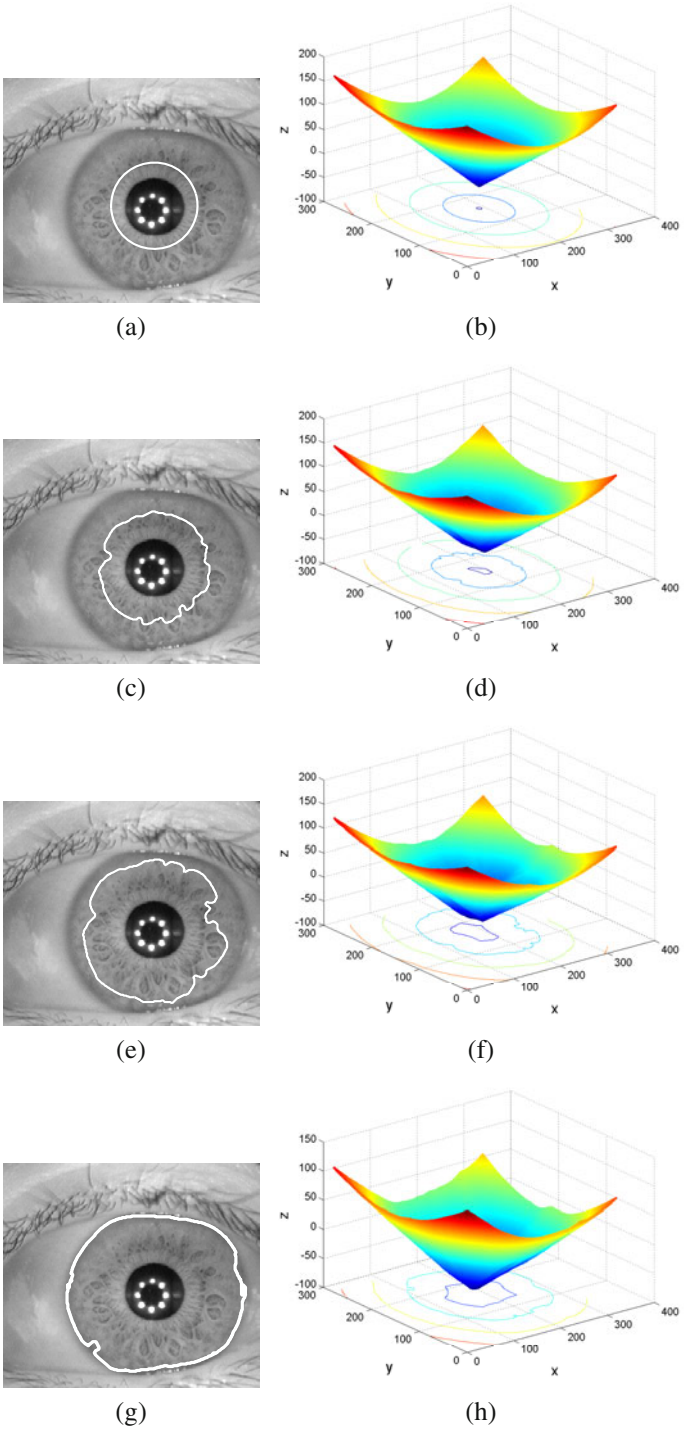


**Fig. 4.12** Evolution of the geodesic active contour during iris segmentation. (a) Iris image with initial contour, (b) embedding function $\psi$ (X and Y axes correspond to the spatial extent of the eye image and the Z axis represents different level sets), (c,d,e,f) contours after 600 and 1400 iterations, and their corresponding embedding functions, and (g,h) Final contour after 1800 iterations (contours shown in white).

curves, then the evolution of the curve might terminate at these local minima. However, geodesic active contours are able to split at such local minima and merge again. Thus, they are able to effectively deal with the problems of local minima, thereby ensuring that the final contour corresponds to the true limbus boundary (Figure 4.13).

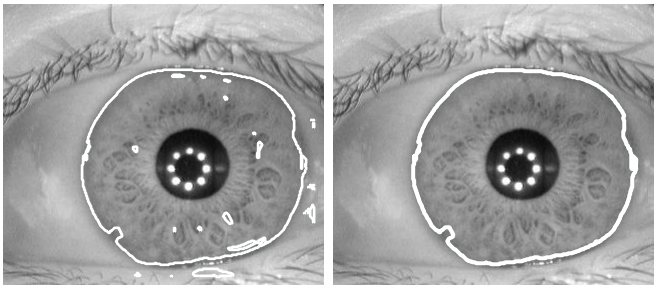

(a) (b)

**Fig. 4.13** The final contour obtained when segmenting the iris using the GAC scheme. (a) Example of a geodesic contour splitting at various local minima, (b) final contour (contours shown in white).

### *4.4.3 Generating iris masks*

The localized iris could potentially be occluded due to other noisy regions such as the eyelashes, shadows, or specular reflections. Thus, a noise mask is generated, which records the locations of such undesired iris occlusions.

## 4.5 Iris Normalization

The amount of iris texture (i.e., its spatial extent) that is revealed in an image can be impacted by a number of factors. Chief among them is the dilation and contraction of the pupil in response to ambient illumination. The size of the iris (i.e., the number of valid iris pixels) increases when the pupil contracts in response to bright light and decreases when the pupil dilates in low light. Apart from this, factors such as the resolution of the sensor and the imaging distance also impact the number of iris pixels that can be gleaned from an image of the eye. Further, the size of the pupil can vary across individuals. To address these variations in size, the segmented iris is unwrapped and converted from cartesian coordinates to a normalized pseudo-polar coordinate system. This normalization operation is performed by representing the segmented iris as a rectangular image, the rows of which correspond to concentric

regions of the iris. This transformation is called Daugmans rubber sheet model and it re-maps every point in the annular region between the two circular boundaries (viz., the pupillary and limbus boundaries) to pseudo-polar coordinates $(r, \theta)$, where $r \in [0,1]$ and $\theta \in [0,2\pi]$, as shown in Figure 4.14.

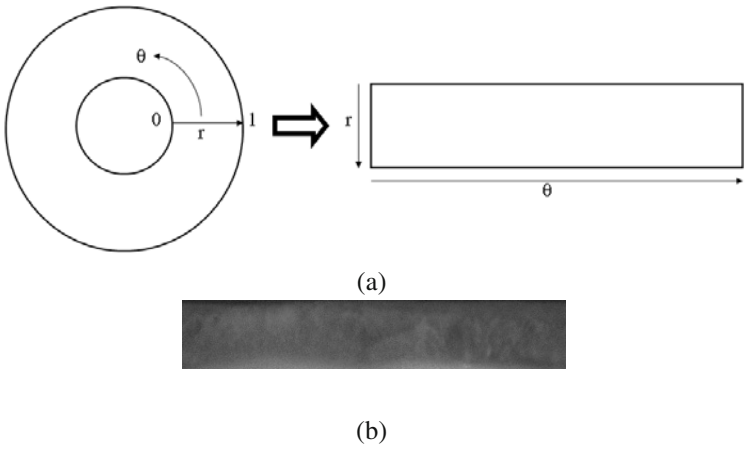


**Fig. 4.14** Iris normalization. (a) Daugman's rubber sheet model is used for iris normalization. The normalization routine converts the pixel coordinates in the annular region between the pupillary and limbus boundaries to polar coordinates. This addresses the problem of variations in pupil size across multiple images. (b) Example of a normalized iris.

The re-mapping of the iris region $I$ from cartesian $(x, y)$ coordinates to the normalized polar coordinates $(r, \theta)$ is expressed as:

$$I(x(r,\theta), y(r,\theta)) \rightarrow I(r,\theta), \tag{4.8}$$

with

$$x(r,\theta) = (1-r)x_p(\theta) + rx_l(\theta), \tag{4.9}$$

and

$$y(r,\theta) = (1-r)y_p(\theta) + ry_l(\theta), \tag{4.10}$$

where $x_p, y_p$ and $x_l, y_l$ are the coordinates of points sampled from the pupillary and limbus boundaries, respectively. Along with the localized iris, the noise masks are also unwrapped to facilitate faster matching.

In order to account for the irregularity and effect of eyelids/eyelashes on the limbus boundary extracted using the GAC scheme, only those points on the contour lying on the boundary of the iris and sclera (as opposed to that of the iris and the eyelids) are used to estimate the radius and center of the iris. Specifically, six points at angles of $[-30^0, 0^0, 30^0, 150^0, 180^0, 210^0]$ with respect to the horizontal axis are selected from the extracted contour and their mean distance from the center of the pupil is used as the approximate radius of the iris ($R$). A circle is next fitted through

all the points on the contour that are within a distance of $R$ pixels from the center of the pupil. This circle estimates the actual limbus boundary of the iris. Figure 4.15 denotes this procedure.

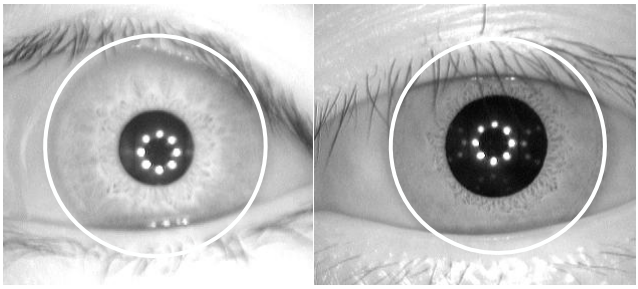

(a) (b)

**Fig. 4.15** When GAC is used to localize the outer iris boundary, then an additional step is needed to facilitate normalization. Thus, the irregular boundary deduced using active contours is converted to a circular boundary as shown in the image above. Those pixels that are included within the circular boundary, but excluded by the irregular boundary are considered to be non-iris pixels and excluded by the mask.

## 4.6 Iris Encoding and Matching

The process of extracting a numerical feature set from the iris is called iris encoding. This corresponds to the feature extraction stage indicated in Chapter 1. To encode the normalized iris texture pattern, a two dimensional Gabor wavelet is usually convolved with the unwrapped iris image. A 2D Gabor wavelet, over an image domain $(x,y)$, is given by:

$$G(x,y) = e^{-\pi[(x-x_0)^2/\alpha^2+(y-y_0)^2/\beta^2]}e^{-2\pi i[(u_0(x-x_0)+v_0(y-y_0)]}, \tag{4.11}$$

where $(x_0,y_0)$ denote the position in the image, $(\alpha,\beta)$ denote the effective width and length, and $(u_0,v_0)$ ascertain the wave direction with a spatial frequency $\omega_0 = \sqrt{u_0^2+v_0^2}$.

The real and imaginary components of this wavelet can be separated as:

$$\Re\{G(x,y)\} = e^{-\pi[(x-x_0)^2/\alpha^2+(y-y_0)^2/\beta^2]}\cos(-2\pi[(u_0(x-x_0)+v_0(y-y_0)]), \tag{4.12}$$

and

$$\Im\{G(x,y)\} = e^{-\pi[(x-x_0)^2/\alpha^2+(y-y_0)^2/\beta^2]}\sin(-2\pi[(u_0(x-x_0)+v_0(y-y_0)]), \tag{4.13}$$

respectively. The real and imaginary outputs obtained by convolving a 2D Gabor wavelet with a normalized iris image are shown in Figure 4.16.

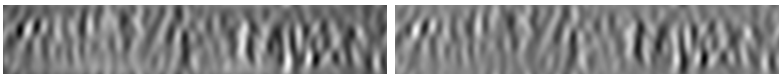

(a) (b)

**Fig. 4.16** Real and imaginary outputs of convolving an image with a 2D Gabor wavelet.

The output of the Gabor wavelets is demodulated to compress the data. This is performed by quantizing the phase information into four different levels, one for each quadrant of the complex plane. As the normalization is earlier performed in the polar coordinates, the wavelet in polar coordinates can be expressed as:

$$H(r,\theta) = e^{-i\omega(\theta-\theta_0)}e^{-(r-r_0)^2/\alpha^2}e^{-i(\theta-\theta_0)^2/\beta^2}, \tag{4.14}$$

where $(r_0,\theta_0)$ denote the center frequency of the wavelet, while all other variables denote the same parameters as in Equation (4.11).

Given the normalized iris image $I(\rho,\phi)$ in the polar coordinate system, the demodulation and phase quantization process can be written as:

$$h_{Re,Im} = sign_{Re,Im}\int_{\rho}\int_{\phi} I(\rho,\phi)e^{-i\omega(\theta_0-\phi)}e^{-(r_0-\rho)^2/\alpha^2}e^{-(\theta_0-\phi)^2/\beta^2}\rho d\rho d\phi, \tag{4.15}$$

where $h_{Re,Im}$ is the complex valued bit whose real and imaginary components are dependent on the sign of the integral. This is illustrated in Figure 4.17. The response of this operation is a binary output referred to as *iris code*. The dimension (or length) of the iris code depends upon the size of the normalized iris image, which in turn depends upon the resolution along the $r$ and $\theta$ axes. A dimension of 2048 is commonly used.

The normalized Hamming Distance (HD) between two iris codes is used as a measure of dissimilarity between two irides. This value is computed by masking every iris code with its respective mask to disregard noisy regions. The Hamming Distance between two iris codes is computed as

$$HD = \frac{\| (IrisCodeA \oplus IrisCodeB) \cap MaskA \cap MaskB \|}{\| MaskA \cap MaskB \|} \tag{4.16}$$

The XOR operator ($\oplus$) detects the bits that disagree between the two iris codes, while the AND operator ($\cap$) masks the noisy regions. The denominator helps in normalizing the total number of bits that disagree in the interval $[0,1]$. A perfect match between two iris codes will result in a HD value of 0. See Figure 4.18.

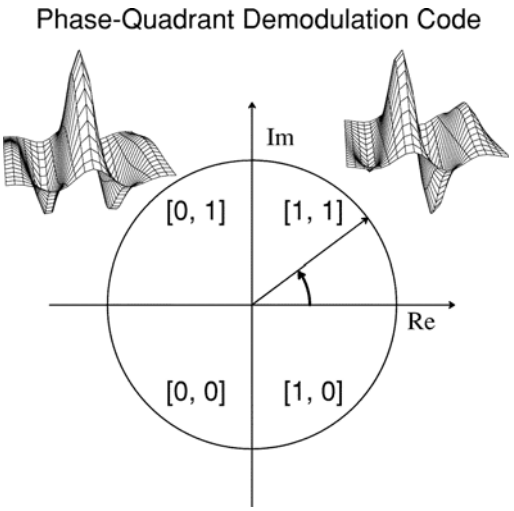


**Fig. 4.17** An illustration of the phase demodulation and quantization process used to encode the iris. The phasor response at each pixel in the normalized iris is quantized into two bits of information.

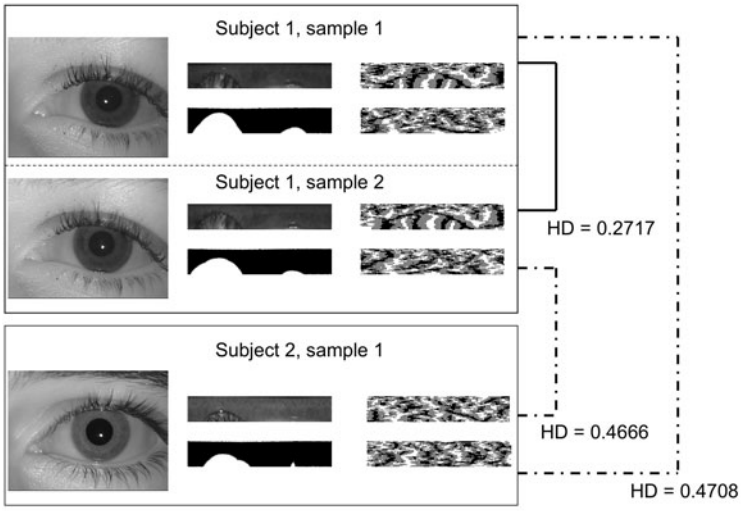


**Fig. 4.18** The process of matching a pair of irides. Here, three images of the eye belonging to two different subjects are shown. Each image is subjected to a segmentation routine in order to extract the iris, which is converted to a rectangular entity via Daugman's rubber sheet model. The segmentation routine results in a binary mask, where a 1 indicates an iris pixel and a 0 indicates a non-iris pixel. The normalized iris is processed using Gabor wavelets and the resulting phasor response is quantized into an iris code. The Hamming Distance (HD) between two iris codes of the same iris is expected to be smaller than that corresponding to two different irides.

## 4.7 Iris Quality

Depending on the field of view of the iris sensor, an iris image usually includes the upper and lower eyelashes and eyelids, and some regions of the eyebrow as shown in Figure 4.19. However, only the rich textural information of the iris between the pupillary and limbus boundaries is used for recognition. Thus, for a given iris image (or a video frame), quality evaluation is typically based on factors that degrade or reduce the size of the iris region.

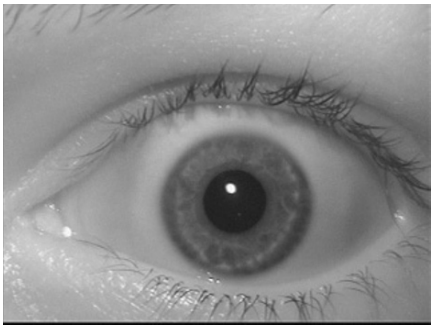

**Fig. 4.19** A sample NIR iris image captured from a cooperative user under near ideal conditions.

Some of the factors that can significantly reduce the quality of an iris image include (a) occlusion, (b) defocus, or out-of-focus, (c) motion blur, (d) non-uniform illumination, (e) low resolution, or large imaging distance, (f) iris dilation, (g) off-angled imaging, and (h) the presence of accessories such as fake or printed contact lenses. Examples are shown in Figure 4.20.

### *4.7.1 Quality assessment techniques*

While most quality evaluation schemes consider only a single or a pair of factors, newer techniques consider a wider range of factors for quality assessment. Some of these are described here.

- Examining the sharpness of a portion between the pupil and iris: Sharpness of an image is usually an indicator of the proper focusing of the object being imaged and thus is usually used in determining the quality of an iris image. Here, sharpness is essentially computed as the normalized magnitude of the intensity gradient near the pupillary boundary. Let $(X_p, Y_p)$ and $r_p$ denote the center and the radius of the pupil, respectively, and $r_i$ denote the radius of the iris. A region of interest is selected such that all the pixels $(x, y)$ lying within the region satisfy the following conditions:

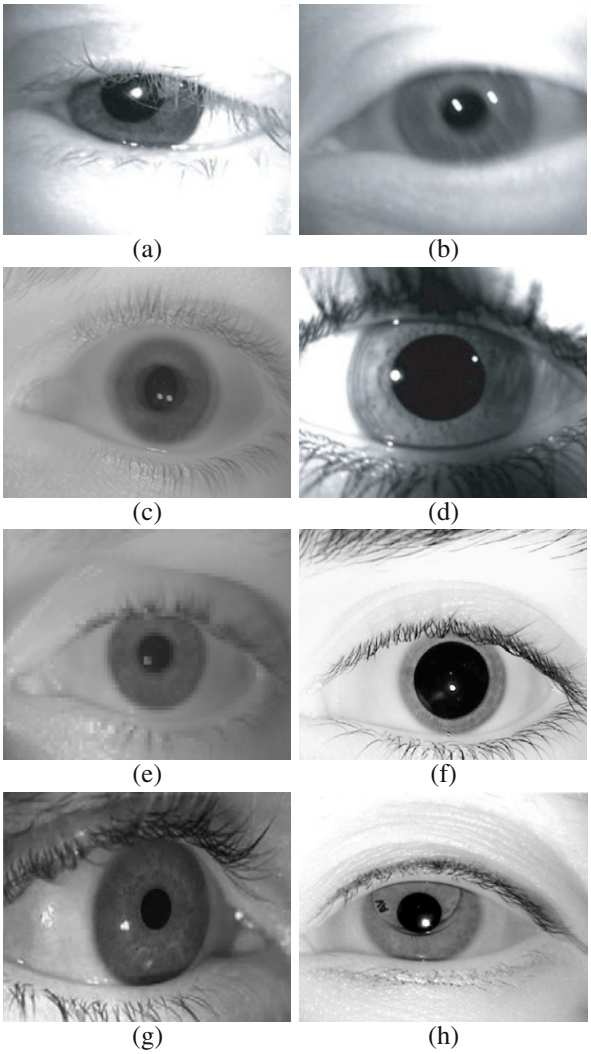


**Fig. 4.20** Poor quality iris images caused by (a) occlusion, (b) defocus, (c) motion blur, (d) non-uniform illumination, (e) low resolution sensor, (f) iris dilation, (g) off-angled imaging, and (h) the presence of a printed contact lens.

$$(y_p - 0.8r_p) < y < (y_p + 0.8r_p) \tag{4.17}$$

and

$$-\sqrt{r_p^2 - (y-y_p)^2} + 0.1r_i < x - x_p < -\sqrt{r_p^2 - (y-y_p)^2} + 0.2r_i \tag{4.18}$$

Figure 4.21 illustrates the region of interest that is specified by the above conditions.

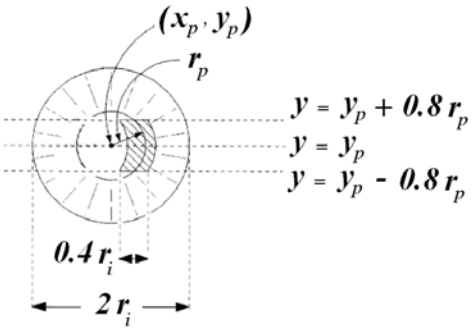


**Fig. 4.21** Region of interest selected for estimating the sharpness of the iris.

From the selected region of interest, the median values of the pixels falling in the pupil region, $M_p$, and the iris region, $M_i$, are computed. Then, for all the pixels in the selected region whose intensity values lie between $M_p$ and $M_i$, the absolute values of their horizontal gradients are gathered in a set. From this set, the average of the top 20 values are computed, and denoted by the variable $S$. The sharpness measure of a given iris image, $\frac{1}{w}$, is then computed by the following equation:

$$\frac{1}{w} = \frac{S}{H}, \tag{4.19}$$

where $H = (M_i - M_p)$, denotes the step size. If the sharpness measure is above a threshold value of 0.5, the image is considered to be well focused and, therefore, of good quality.

- Quantifying the energy of high spatial frequencies over the entire image: This method determines the sharpness over the whole image using 2D Fourier analysis in order to eliminate optically defocused images.
  For a given image represented as a 2D function of the real plane $I(x,y)$, its 2D Fourier transform $F(\mu,\nu)$ is defined by:

$$F(\mu,\nu) = \frac{1}{(2\pi)^2}\int\int I(x,y)\exp(-i(\mu x+\nu y))dxdy. \tag{4.20}$$

  The defocused image, $D_\sigma(\mu,\nu)$, is related to the 2D Fourier transform of the corresponding in-focus image, $F(\mu,\nu)$, by the following model:

$$D_\sigma(\mu,\nu) = \exp\left(-\frac{\mu^2+\nu^2}{\sigma^2}\right)F(\mu,\nu). \tag{4.21}$$

  Defocusing primarily attenuates the highest frequencies in the image, while the lower frequency components are virtually unaffected. This is because the expo-

nential term in the above equation approaches to unity as the frequencies $(\mu, \nu)$ become small. Thus, an effective method of identifying a defocused image would be to simply measure its total power in the 2D Fourier domain at higher spatial frequencies (as they are most attenuated by defocus). To make this quality measure independent of the image content, the ratio of power of the higher frequency bands may be compared to that of the lower frequency bands.

- Analyzing the Fourier spectra of local iris regions: This can be used to detect poor quality images caused by factors such as (a) out-of-focus blur, (b) motion blur, and (c) occlusion due to the eyelashes, and/or eyelids. The Fourier analysis of a given iris image yields a significant amount of information, which can be used to isolate poor quality images from a given set of images. For an out-of-focus image, the Fourier spectrum is supposed to be largely dominated by the low frequency components. On the other hand, an iris image with occlusions contains significant middle and high frequency components that are caused by the eyelashes. The Fourier spectrum of a motion blurred image lacks middle and high frequency components, and has frequency distribution similar to that of an out-of-focus image.
  The descriptor used for estimating the quality of an iris image can then be defined as:

$$D = \left[ (F_1 + F_2 + F_3); \frac{F_2}{F_1 + F_3} \right], \tag{4.22}$$

  where

$$F_i = \int\int_{\Omega = \{(u,v) | f_1^i < \sqrt{u^2+v^2} <= f_2^i\}} | F(u,v) | \, du dv \quad i = 1,2,3, \tag{4.23}$$

  and $F(u,v)$ is the 2D Fourier spectrum of the iris region, while $F_1$, $F_2$, and $F_3$ denote the power of the low, middle, and high frequency components, respectively. Frequencies $f_1^i$ and $f_2^i$ are the radial frequency pair, that form the extrema of the corresponding frequency components.
  The quality descriptor $D$ consists of two discriminating frequency features. The first feature is the total spectrum power of the iris region that can effectively discriminate severely occluded iris images from high quality images. The second feature is a ratio of the middle frequency power to the other frequency powers. For a clearly focused image, this ratio is high, when compared to out-of-focus or motion blurred images.
  For a given iris image, $I$, two $64 \times 64$ regions are selected as shown in Figure 4.22, and the quality descriptor values are computed. The mean of the resulting two local quality descriptors is regarded as an appropriate quality measure of the iris image.
- Measuring the energy from 2D wavelets at local concentric bands of iris: This approach evaluates the quality of a given iris image using 2D wavelets on local concentric bands of a segmented iris. The local quality measure is then used as a

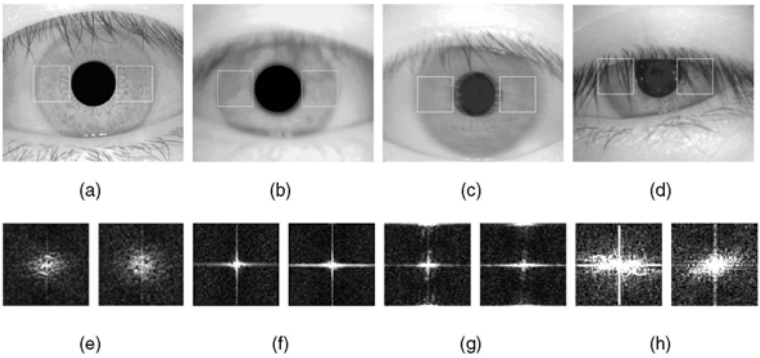


**Fig. 4.22** (a) An iris image of good quality. Poor quality iris images, caused by (b) out-of-focus, (c) motion blur, and (d) occlusion. The images (e), (f), (g), and (h) show the Fourier spectra of the selected two local iris regions of size $64 \times 64$ (highlighted by the white boxes), corresponding to images (a), (b), (c), and (d), respectively. Image reproduced from [23]. ©IEEE.

weighting scheme in the matching process to yield improved results. The analysis is performed on local regions since the quality can vary from region to region. Thus, the method uses higher weights for inner regions of the iris that are more stable compared to the outer regions that are more prone to occlusions.
Given an image $I(x,y) \in R^2$, its Continuous Wavelet Transform (CWT), defined as the convolution with a series of wavelet functions, is given by the following equation:

$$w(s,x_0,y_0) = \frac{1}{\sqrt{s}} \int\int_{R^2} I(x,y)\phi\left(\frac{x-x_0}{s}, \frac{y-y_0}{s}\right)dxdy, \tag{4.24}$$

where $s$ is the dilation (scale) factor, and $(a,b)$ denotes the translation (shift) factor. The wavelet $\phi$ is considered to be a Mexican hat wavelet, which is essentially a band pass filter for edge detection at scales $s$. The choice of the wavelet is due to its high sensitivity to features exhibiting sharp variations (e.g., pits, freckles, etc.) and non-linearity (e.g., collarette, furrows, etc.). First, in order to capture various features at multiple scales, the product responses are obtained, given by the following equation:

$$w^{mul}(s_1,s_2,s_3) = w(s_1) \times w(s_2) \times w(s_3). \tag{4.25}$$

Here, $s_1$, $s_2$, $s_3$ are three considered scales. To perform quality evaluation of an iris image, the iris is segmented to obtain the boundaries of the pupil and iris. The segmented iris is then partitioned into multiple concentric bands of fixed width, which are centered at the pupil center.
To obtain the local quality measure, the energy $E_t$ of the $t$-th band $(t = 1,2,...T)$, where $T$ denotes the total number of bands, is computed by the following equation:

$$E_t = \frac{1}{N_t} \sum_{i=1}^{i=N_t} | w_{t,i}^{mul} |^2, \tag{4.26}$$

where $w_{t,i}^{mul}$ represents the $i$-th product based wavelet coefficient in the $t$-th band, and $N_t$ is the total number of wavelet coefficients in the $t$-th band. The energy, $E_t$, is considered as a good indicator of the distinctiveness of the iris features, and is therefore a reliable measure of the local quality. A high value of $E_t$ suggests a good quality image.

The quality index of the entire iris image, $Q$, is defined as the weighted average of the band-wise local quality values, and is given by:

$$Q = \frac{1}{T} \sum_{t=1}^{T} (m_t \times \log(E_t)), \tag{4.27}$$

where $T$ represents the total number of bands and $m_t$ is the weight, given by $m_t = \exp\{- \| l_t - l_c \|^2 / (2q)\}$. The variable $l_c$ denotes the center of the pupil, and $l_t$ denotes the mean radius of the $t$-th band with respect to $l_c$.

To incorporate local quality measures into the matching scheme, Daugman's Hamming distance matching algorithm is modified as:

$$HD_w = \frac{1}{B} \frac{\sum_{i=1}^{B} \sqrt{E_{g(i)}^X \times E_{g(i)}^Y} \times (X_i \bigotimes Y_i)}{\sum_{i=1}^{B} \sqrt{E_{g(i)}^X \times E_{g(i)}^Y}}, \tag{4.28}$$

where $X_i$ and $Y_i$ represent the $i$-th bit of the iris code sequences $X$ and $Y$, respectively, and $N$ is the total number of bits in the sequence. $g(i)$ is the index of the band that contains the $i$-th bit of the IrisCode, and $E_{g(i)}^X$ and $E_{g(i)}^Y$ are the local quality measures of the $g(i)$-th band in $X$ and $Y$, respectively. The symbol $\bigoplus$ represents the logical XOR operation.

Iris image quality assessment is an area of continuing research. While initial research has shown the benefits of incorporating iris quality, its assessment and use in a real-time environment is still an open challenge.

## 4.8 Performance Evaluation

According to the biometric literature, the structural texture in the iris is substantially diverse across the population. As stated before, even the irides of monozygotic twins exhibit structural differences. Large-scale testing has confirmed the potential of iris patterns to identify individuals in a large database of subjects. Experiments conducted by Daugman on a database of 632,500 iris images (316,250 persons spanning 152 nationalities) suggest the possibility of a decision policy that could yield zero error rates. However, this rate is predicated on the quality of the iris image, which must be strictly monitored to ensure reasonable textural clarity. Tests conducted in

2006 by the National Institute of Standards and Technology involving a broad range of image quality suggest that the false nonmatch rate of the best performing iris recognition algorithms can vary between 1.1 to 1.4 percent at a false match rate of 0.1 percent.

## 4.9 Summary

The tremendous progress in iris recognition systems has resulted in several challenges and new opportunities, which have been the focus of recent research efforts. We conclude this chapter by listing some of these challenges.

- The iris is a moving object with a small surface area, residing within an eyeball that can move independently of the iris. The eyeball in turn is within the head, another moving object. The formidable challenge, therefore, is to reliably locate the eyeball and localize the iris's position in images obtained at a distance from unconstrained human subjects. Because acquisition modules typically image the iris in the NIR spectrum, appropriate invisible lighting is required to illuminate the iris while acquiring the image. These factors confound the system's ability to operate successfully when the subject is more than a few meters away from the camera. Recent efforts have successfully designed and developed iris-on-the-move and iris-at-a-distance recognition systems. Other efforts are investigating technologies such as wavefront-coded imaging to increase the camera's depth of field.
- Nonideal irides can result from motion blur, camera diffusion, transmission noise, out-of-focus imaging, occlusion from eyelids and eyelashes, head rotation, off-axis gaze or camera angle, specular reflection, poor contrast, and natural luminosity - factors that can lead to a higher false nonmatch rate. Robust image restoration schemes are needed to enhance the quality of such iris images before the system processes them. Recent research has attempted to deal with the problem of off-axis iris images by designing suitable calibration and geometric correction models.
- A common assumption is that the textural relief of an iris is unique because of its random morphogenesis, and large-scale empirical evaluations have confirmed this notion across a large segment of the population. However, no effective theoretical models exist for quantifying the iris's individuality. Although researchers have used match-score distributions and IrisCode statistics to infer the iris biometric's degrees of freedom, no one has yet directly used the iris's biological underpinnings to ascertain its individuality. This interesting problem has implications for using iris recognition in a court of law in accordance with Daubert's admissibility criteria and Federal Rules of Evidence.
- By combining the iris with other ocular features such as conjunctival vasculature, researchers might be able to develop robust ocular-based multibiometric systems that can operate in environments characterized by harsh lighting, moving subjects, and large stand-off distances. Explicitly combining ocular features

with local facial attributes such as skin texture and facial marks in the periocular region (the region around the eye) can enhance the performance of face-based biometric systems. Using the iris in a multimodal framework can enhance matching accuracy and reduce constraints on the depth of field by allowing the use of low-resolution iris images.

- The use of biometric systems in large-scale government and civilian applications has raised concerns about the iris template's security and the retention of its owner's privacy. Security and privacy are of particular concern in centralized databases, which can store millions of iris templates. Privacy-enhancing technology, along with cancelable biometrics (see Chapter 7, Security of Biometric Systems), is likely to raise the privacy and security levels of such personal information. However, more research is required to incorporate these schemes in an operational environment.

Despite its challenges, iris recognition is gaining popularity as a robust and reliable biometric technology. The iris's complex texture and its apparent stability hold tremendous promise for leveraging iris recognition in diverse application scenarios, such as border control, forensic investigations, and cryptosystems. The use of other ocular features and facial attributes along with the iris modality could enable biometric recognition at a distance with excellent matching accuracy. The future of iris-based recognition looks bright, particularly in military applications that demand the rapid identification of individuals in dynamic environments.

## Bibliographical and Historical Remarks

The possibility of using the iris[6] as a cue for human recognition or categorization was suggested by various individuals, including French police officer Alphonse Bertillon in 1885 [2], American ophthalmologist Frank Burch in 1936 and British ophthalmologist James Doggart in 1949 [14]. In 1987, American Ophthalmologists Leonard Flom and Aran Safir were issued a patent for designing a conceptual framework for automated iris recognition [15]. However, their patent did not include a specific procedure for feature extraction and matching and was, therefore, a broad generalization of the process for automated iris recognition. A few years later, at the suggestion of Flom and Safir, renowned computer vision scientist John Daugman actually designed and evaluated a method for automated iris recognition [11, 6]. To this day, many of the algorithms originally designed by Daugman are still being used in commercial iris recognition systems.

Daugman employed the integro-differential operator for localizing the inner and outer contours of the iris. He introduced the rubber sheet model to transform the iris from an annular structure to a normalized fixed-size rectangular entity; this was an elegant way of accommodating variations in iris diameter and head tilt whilst ensuring ease of matching. He used 2-D Gabor filters [10] for examining the texture

[6] The word *iris* is derived from the Greek word ιρις meaning "rainbow"

of the normalized iris image. The term "iris code", that refers to the binarized phasor response obtained when the normalized iris image is convolved with a Gabor filter, is also due to Daugman [11]. A rigorous treatment of iris codes can be found in [12, 22]. The work in [20] established that some bits in the iris code are more consistent than the others. The use of iris codes in designing biometric cryptosystems and indexing schemes has also been demonstrated [17, 18].

In 1994, Wildes et al. [36] suggested the use of the Generalized Hough Transform for iris segmentation. The proposed technique relied on the use of gradient-based edge detectors to process the input eye image prior to invoking the Hough-based voting scheme for detecting the pupillary boundary, the limbus boundary and the eyelid contours. Feature extraction was performed on the segmented iris image using a four-band Laplacian-of-Gaussian filter, and the normalized cross-correlation values between corresponding bands were used to compare two irides [37].

Apart from the integro-differential operator and the Hough Transform method, other approaches to iris segmentation include those based on Fourier Series [13], Geodesic Active Contours [33], Fuzzy Clustering [29], and Elastic Models [19]. The use of alternate feature encoding and matching schemes, other than the classical wavelet-based methods, have also been investigated. Examples include those based on Ordinal Features [34], Scale Invariant Feature Transforms [1] and Correlation Filters [35]. A survey of other approaches to iris recognition can be found in [3].

Methods for processing off-axis iris images, in which the eye gaze is directed away from the camera, have been discussed in [32]. While iris processing has been traditionally done in the near-infrared spectrum, recent work has explored the possibility of acquiring and processing iris images in the visible spectrum and the short-wave infrared spectrum [4, 27, 31, 24]. The benefits of multispectral iris analysis are likely to be realized in future iris recognition systems.

The issue of image quality is of paramount importance due to its impact on both iris segmentation and feature encoding. A detailed reading list is available in the NIST Biometrics Quality Homepage currently hosted at `http://www.nist.gov/itl/iad/ig/bio_quality.cfm`. Evaluation of iris recognition algorithms have been conducted as part of *Independent Testing of Iris Recognition Technology* (ITIRT [21]), *Iris Challenge Evaluation* (ICE [25, 26]), *Multibiometric Grand Challenge* (MBGC), *Iris Exchange Evaluation* (IREX [16]) and *Noisy Iris Challenge Evaluation* (NICE [28]).

## References

1. C. Belcher and Y. Du. Region-based sift approach to iris recognition. *Optics and Lasers in Engineering*, 47(1):139–147, 2009.
2. A. Bertillon. La couleur de l'iris. *Revue Scientifique*, 1885.
3. K. Bowyer, K. Hollingsworth, and P Flynn. Image understanding for iris biometrics: a survey. *Computer Vision and Image Understanding*, 110(2):281–307, 2008.
4. C. Boyce, A. Ross, M. Monaco, L. Hornak, and X. Li. Multispectral iris analysis: A preliminary study. In *Proc. of IEEE Computer Society Workshop on Biometrics at the Computer Vision and Pattern Recognition (CVPR) Conference*, New York, USA, June 2006.

5. Y. Chen, S. Dass, and A. K. Jain. Localized iris quality using 2-d wavelets. In *Advances in Biometrics*, pages 373–381. Springer, 2005.
6. J. Daugman. Biometric personal identification system based on iris analysis. United States Patent 5291560, March 1994.
7. J. Daugman. How iris recognition works. *IEEE Transactions on Circuits and Systems for Video Technology*, 14(1):21–30, January 2004.
8. J. Daugman. Probing the uniqueness and randomness of iriscodes: Results from 200 billion iris pair comparisons. *Proceedings of IEEE*, 94(11):1927–1935, 2006.
9. J. Daugman and C. Downing. Epigenetic randomness, complexity, and singularity of human iris patterns. *Proceedings of Royal Society Biological Sciences*, B(268):1737–1740, 2001.
10. J. G. Daugman. Two-dimensional spectral analysis of cortical receptive field profiles. *Vision Research*, 20(10):847–856, 1980.
11. J. G. Daugman. High confidence visual recognition of persons by a test of statistical independence. *IEEE Transactions on Pattern Analysis and Machine Intelligence*, 15(11):1148–1160, November 1993.
12. J. G. Daugman. The importance of being random: Statistical principles of iris recognition. *Pattern Recognition*, 36(2):279–291, 2003.
13. J. G. Daugman. New methods in iris recognition. *IEEE Trans. on System, Man, and Cybernetics, Part B*, 37(5):1167–1175, 2007.
14. J. H. Doggart. *Ocular Signs in Slit-lamp Microscopy*. Kimpton, London, 1949.
15. L. Flom and A. Safir. Iris recognition system. United States Patent 4641349, February 1987.
16. P. Grother, E. Tabassi, G. W. Quinn, and W. Salamon. IREX I: Performance of iris recognition algorithms on standard images. Technical Report NISTIR 7629, National Institute of Standards and Technology, October 2009.
17. F. Hao, R. Anderson, and J. Daugman. Combining crypto with biometrics effectively. *IEEE Transactions on Computers*, 55:1081–1088, September 2006.
18. F. Hao, J. Daugman, and P. Zielinski. A fast search algorithm for a large fuzzy database. *IEEE Transactions on Information Forensics and Security*, 3(2):203–212, June 2008.
19. Z. He, T. Tan, Z. Sun, and X. Qiu. Towards accurate and fast iris segmentation for iris biometrics. *IEEE Transactions on Pattern Analysis and Machine Intelligence*, 31(9):1670–1684, September 2009.
20. K. P. Hollingsworth, K. W. Bowyer, and P. J. Flynn. The best bits in an iris code. *IEEE Transactions on Pattern Analysis and Machine Intelligence*, 31(6):964–973, June 2009.
21. International Biometric Group. Independent testing of iris recognition technology. Technical report, 2005.
22. A. W. K. Kong, D. Zhang, and M. .S. Kamel. An analysis of iriscode. *IEEE Transactions on Image Processing*, 19(2):522–532, February 2010.
23. L. Ma, T. Tan, Y. Wang, and D. Zhang. Personal identification based on iris texture analysis. *IEEE Transactions on Pattern Analysis and Machine Intelligence*, 25(12):1519–1533, December 2003.
24. H.T. Ngo, R.W. Ives, J.R. Matey, J. Dormo, M. Rhoads, and D. Choi. Design and implementation of a multispectral iris capture system. In *Forty-Third Asilomar Conference onSignals, Systems and Computers*, pages 380 –384, November 2009.
25. P. J. Phillips, K. W. Bowyer, P. J. Flynn, X. Liu, and W. T. Scruggs. The iris challenge evaluation 2005. In *IEEE Second International Conference on Biometrics: Theory, Applications and Systems*, Crystal City, USA, September/October 2008.
26. P. J. Phillips, W. T. Scruggs, A. J. OToole, P. J. Flynn, K. W. Bowyer, C. L. Schott, and M. Sharpe. FRVT 2006 and ICE 2006 large-scale results. Technical Report NISTIR 7408, National Institute of Standards and Technology, March 2007.
27. H. Proença. Iris recognition: On the segmentation of degraded images acquired in the visible wavelength. *IEEE Transactions on Pattern Analysis and Machine Intelligence*, 32(8):1502 – 1516, August 2010.
28. H. Proença and L. A. Alexandre. The NICE I: Noisy iris challenge evaluation - part I. In *IEEE International Conference on Biometrics: Theory, Applications, and Systems*, Washington DC, USA, September 2007.

29. H. Proença and L.A. Alexandre. Iris segmentation methodology for non-cooperative recognition. *IEE Proceedings - Vision, Image, and Signal Processing*, 153(2):199–205, 2006.
30. A. Ross. Iris recognition: The path forward. *IEEE Computer*, pages 30–35, February 2010.
31. A. Ross, R. Pasula, and L. Hornak. Exploring multispectral iris recognition beyond 900nm. In *Proc. of 3rd IEEE International Conference on Biometrics: Theory, Applications and Systems*, Washington DC, USA, September 2009.
32. S. Schuckers, N. Schmid, A. Abhyankar, V. Dorairaj, C. Boyce, and L. Hornak. On techniques for angle compensation in nonideal iris recognition. *IEEE Trans. on System, Man, and Cybernetics, Part B*, 37(5):1176–1190, 2007.
33. S. Shah and A. Ross. Iris segmentation using geodesic active contours. *IEEE Transactions on Information Forensics and Security*, 4(4):824–836, 2009.
34. Zhenan Sun and Tieniu Tan. Ordinal measures for iris recognition. *IEEE Transactions on Pattern Analysis and Machine Intelligence*, 31(12):2211–2226, December 2009.
35. J. Thornton, M. Savvides, and B. V. K. Vijaya Kumar. Robust iris recognition using advanced correlation techniques. In *Second International Conference on Image Analysis and Recognition (ICIAR)*, volume 3656, pages 1098–1105, Toronto, Canada, September 2005. Springer Berlin / Heidelberg.
36. R. Wildes, J. Asmuth, G. Green, S. Hsu, R. Kolczynski, J. Matey, and S. Mcbride. A system for automated iris recognition. In *Proceedings of the Second IEEE Workshop on Applications of Computer Vision*, pages 121–128, 1994.
37. R. P. Wildes. Iris recognition: An emerging biometric technology. *Proceedings of the IEEE*, 85(9):1348–1363, September 1997.
38. G. Zhang and M Salganicoff. Method of measuring the focus of close-up image of eyes. United States Patent 5953440, 1999.